Colloids and Surfaces B: Biointerfaces 207 (2021) 112037

Contents lists available at ScienceDirect

Colloids and Surfaces B: Biointerfaces

journal homepage: www.elsevier.com/locate/colsurfb

TiO_2@BSA nano-composites investigated through orthogonal multi-techniques characterization platform

Simona Ortelli [a,*], Anna L. Costa [a,*], Ilaria Zanoni [a], Magda Blosi [a], Otmar Geiss [b], Ivana Bianchi [b], Dora Mehn [b], Francesco Fumagalli [b], Giacomo Ceccone [b], Giuditta Guerrini [c], Luigi Calzolai [b]

[a] ISTEC-CNR, Institute of Science and Technology for Ceramics-National Research Council of Italy, Via Granarolo 64, Faenza, RA, Italy
[b] European Commission, Joint Research Centre, Directorate F Health, Consumers and Reference Materials, Ispra, VA, Italy
[c] Laboratory of Molecular Microbiology and Biotechnology, Department of Medical Biotechnologies, University of Siena, Viale Bracci 16, 53100, Siena, Italy

ARTICLE INFO

Keywords:
Multi-techniques characterization platform
Colloidal approach
TiO_2 nanoparticle
BSA coating
Safe-by-design

ABSTRACT

Biocompatible coating based on bovine serum albumin (BSA) was applied on two different TiO_2 nanoparticles (aeroxide P25 and food grade E171) to investigate properties and stability of resulting TiO_2@BSA composites, under the final perspective to create a "Safe-by-Design" coating, able to uniform, level off and mitigate surface chemistry related phenomena, as naturally occurring when nano-phases come in touch with proteins enriched biological fluids. The first step towards validating the proposed approach is a detailed characterization of surface chemistry with the quantification of amount and stability of BSA coating deposited on nanoparticles' surfaces. At this purpose, we implemented an orthogonal multi-techniques characterization platform, providing important information on colloidal behavior, particle size distribution and BSA-coating structure of investigated TiO_2 systems. Specifically, the proposed orthogonal approach enabled the quantitative determination of bound and free (not adsorbed) BSA, a key aspect for the design of intentionally BSA coated nano-structures, in nanomedicine and, overall, for the control of nano-surface reactivity. In fact, the BSA-coating strategy developed and the orthogonal characterisation performed can be extended to different designed nanomaterials in order to further investigate the protein-corona formation and promote the implementation of BSA engineered coating as a strategy to harmonize the surface reactivity and minimize the biological impact.

1. Introduction

The presence of endogenous or exogenous coating on highly exposed surface of nanomaterials (NMs), dictates their interactions with the surrounding physicochemical and biological environment and as consequence influence their Environment, Health and Safety (EHS) profiles [1,2]. Therefore, there is a growing interest to accurately characterize the nanoparticles (NPs) coating and many studies addressed the characterization of protein-corona, deriving by biomolecules adsorption on NPs surface [3–6]. Serum albumins are the most abundant proteins in the blood plasma and play an important role in many important functions, for the transport of various endogenous and exogenous ligands [7], for the solubilization and detoxifycation of common toxicants, such as heavy metals, reactive oxygen species and ions, in blood plasma [8]. Bovine serum albumin (BSA), having 76 % homology with human serum albumin (HSA), has been regarded as a promising material in nanomedicine [9] for its low cost, biodegradability, nontoxicity, non-immunogenicity, water solubility, high ligand-binding properties, intrinsic fluorescence, stability to pH and temperature, wide acceptance in pharmaceutical industry [9,10]. Different strategies for the conjugation of NPs with albumin have been described from covalent or non-covalent interactions by self-assembling (passive adsorption) [11], to covalent interactions between functionalised BSA (carboxylated, thiolated, surface charge modified) and NPs surface molecules (active adsorption) [12], to sol-gel routes where BSA acts as reducing/capping/emulsifying agent [13]. Nevertheless, in order to further validate BSA-coating as design tool in nanomedicine, in nanotoxicology (bio-corona model, dispersing agent) and overall, as safe-by-design strategy in nanomanufacturing, we looked for a simple and easily scalable colloidal process, validated through a robust and

* Corresponding authors.
E-mail addresses: simona.ortelli@istec.cnr.it (S. Ortelli), anna.costa@istec.cnr.it (A.L. Costa).

https://doi.org/10.1016/j.colsurfb.2021.112037
Received 9 March 2021; Received in revised form 30 June 2021; Accepted 12 August 2021
Available online 14 August 2021

multi-technique characterisation approach.

In general, the characterization of surface chemistry, closely connected to coating composition and thickness, remains a very challenging objective, because quantitative measurements are difficult to perform in-situ and require the use of specialized instruments, that are not widely available or easy to use and interpret [14]. Several techniques have been widely used and standardized to characterize fundamental parameters as size, crystal structure, elemental composition and a variety of other physicochemical properties of NMs. Nevertheless, despite many studies and published papers, still lacking standardized protocols for the advanced characterization of organic, inorganic, proteins-based coatings [15–17]. Our approach was developed in front of the increasing concerns about titanium oxide safety and possible adverse immuno and genotoxicity outcomes, due to TiO_2 NPs exposure [18–20].

The more general idea is to apply a stable BSA-coating on NPs in order to uniform the surface reactivity and let NPs exposing the same biocompatible surface. We investigated the surface modification occurring when BSA-coating is forming via colloidal self-assembling on differently charged TiO_2 NPs (positively charged P25 and negatively charged E171).

An orthogonal multi-techniques characterization platform was implemented for the separation, detection and characterisation of bound and unbound BSA. A quantitative estimation was possible through asymmetric-flow field flow fractionation (AF4) or ultracentrifugation combined with UV/VIS spectroscopy or thermal gravimetric analysis (TGA). Moreover, we used X-ray photoelectron spectroscopy (XPS) to characterize the chemistry of very thin surface layers and Fourier transform infrared spectroscopy-attenuated total reflectance (FTIR-ATR) to obtain information about secondary structure of BSA and its modification once adsorbed on NPs surface. In addition, an in-depth colloidal characterization was carried out by comparing different techniques for determining particle size distribution and surface charge.

2. Materials and methods

2.1. Materials

Titanium dioxide Aeroxide®P25 (P25) nanopowder was purchased by Evonik. Food grade titania Hombitan FG (E171), produced by Venator, was provided by Korea Research Institute of Standards and Science (KRISS). The dissolved ionic gold and titanium standard (1 g L^{-1} in 5% HCl and 2% HNO_3 respectively), bovine serum albumin, hydrochloric acid, glucose and sodium hydroxide were purchased from Sigma-Aldrich. Gold nanoparticles with a nominal diameter of 63 nm (43.45 μg mL^{-1} in aqueous 2 mM sodium citrate) and phosphate-buffered saline were purchased from NanoComposix and Thermo Fisher Scientific, respectively.

2.2. Preparation of TiO_2@BSA samples

P25 and E171 powders were dispersed in ultrapure water at a concentration of 0.1 wt% by bath sonicating for 10 min. BSA solutions were prepared by dissolving the powder in ultrapure water under magnetic stirring at room temperature. BSA solutions were dripped drop by drop on P25 and E171 nanosuspensions to a BSA:TiO_2 weight ratio equal to 0.3 and 0.6, respectively. The samples were mixed under magnetic stirring overnight, obtaining P25@BSA and E171@BSA nanosols samples. As regards E171 NPs, showing negative surface charge, at natural pH, we slightly acidified BSA solution (pH range 3.5÷4.0, adding few drops of HCl 0.1 M) in order to promote the heterocoagulation with positively charged BSA. Spray-freeze-drying (SFD), was applied in order to force the physicochemical interaction between the two phases, BSA and TiO_2, due to water solvent removal (see ESI - "Production of spray-freeze-dried samples" and Figure S1) [21], producing a highly porous granulated powder and obtaining P25 SFD, P25@BSA SFD, E171 SFD and E171@BSA SFD samples.

2.3. Analytical characterization

2.3.1. Single particle ICP-MS

Single particle analysis of pristine P25 and E171 nanosuspensions in water has been performed by Single Particle Inductively Coupled Plasma–Mass spectrometry (sp-ICPMS). A Perkin Elmer NexIon 300D quadrupole ICPMS, equipped with an SC Fast peristaltic pump, a Meinhard concentric nebuliser, a glass cyclonic spray chamber and a standard quartz torch (2.5 mm i.d) operating in standard mode was used (Perkin Elmer, Waltham, MA, US), coupled with the Nano Application Module of the Syngistix™ software for the setting of all parameters and data acquisition. The dwell time was set at 100 μs and the total data acquisition time at 60 s. The transport efficiency was determined following the 'particle size' approach [22,23]. A 63 nm gold NPs suspension with a concentration of approximately 100,000 particles mL^{-1} and solutions of dissolved gold (blank and four solutions ranging from 1 to 10 μg L^{-1}) were prepared by diluting the stock solutions with ultrapure water and used as standard for NPs size dimension in Single-Particle software calibration material. The transport efficiency was 11.8 %. For the determination of titanium dioxide nanoparticles, the isotope ^{48}Ti was monitored setting the mass fraction to 60 % and density to 3.9 g cm^{-3}. A 5-point curve ranging from 0 to 15 μg L^{-1} dissolved titanium in 1% HNO_3 was used for calibration. Samples were prepared suspending 30 mg of E171 and P25, as powders, in 30 mL of ultrapure water. Suspensions were bath sonicated at the maximum power for 600 s and then diluted 1:100000 and 1:1000 in ultrapure water, respectively immediately before the analysis.

2.3.2. X-ray diffraction

XRD measurements were carried out on pristine powder P25 and E171 at room temperature with a Bragg/Brentano diff ;ractometer (X'pertPro PANalytical) equipped with a fast X'Celerator detector, using a Cu anode as the X-ray source (Kα, λ = 1.5418 Å). Diff ;ractograms were recorded in the range 20−80°2θ counting for 0.2 s every 0.05 ° 2θ step.

2.3.3. Dynamic and electrophoretic light scattering

The hydrodynamic diameter (d_{DLS}) and Zeta potential (Z-pot_{ELS}) were determined by dynamic and electrophoretic light scattering measurements, respectively, using a Zetasizer nano ZSP (model ZEN5600, Malvern Instruments, UK). Samples were measured three times and data were obtained by averaging the three measurements. In order to better investigate the colloidal behaviour and the affinity between TiO_2 and BSA phases, Z-pot versus pH or BSA added, were carried out using the instrument coupled with an automatic titrating system. The technique was applied to TiO_2 and TiO_2@BSA nanosols, even after ultracentrifugation (UC) for TiO_2@BSA UC samples. All the details related to samples preparation were reported in ESI (Electrophoretic light scattering).

2.3.4. Effective density by volumetric centrifugation

1 mL sample suspensions of pristine TiO_2 and TiO_2@BSA nanosols (P25@BSA and E171@BSA) were dispersed into TPP PCV tubes (Techno Plastic Products, Trasadingen, Switzerland) and centrifuged at 2500 *g* for 30 min using MicroCL 21 Centrifuge (Thermo Scientific). Agglomerate sediment volume, V_{sed}, was measured using a slide rule-like easy-measure device also obtained from the PCV tube manufacturer. Effective density (ρ^e_A) was calculated from V_{sed} using the Equation (1)

$$\rho_A^e = \frac{m_P^A}{V_{sed} SF}\left(1 - \frac{\rho_L}{\rho_P}\right) + \rho_L \quad (1)$$

where m^A_P is the mass of NPs in the agglomerates; V_{sed} is the volume of sediment, measured with volumetric centrifugation method (VCM); SF is the stacking fraction, i.e., fraction of agglomerates in the sediment, it depends on the efficiency of agglomerate stacking, we consider SF values to approximate the theoretical value for random close stacking

(0.634) [24]; ρ_L is the liquid density and ρ_P is the NPs density.

2.3.5. Disk centrifuge sedimentation

Centrifugal liquid sedimentation (CLS) analysis of the samples was performed to determine particle size distributions. CLS measurements were performed using a line start disc centrifuge (CPS Instruments Europe, Oosterhout, The Netherlands) equipped with a 405 nm laser, using two different sucrose gradients, 0–8 %wt and 8–24 %wt, at a rotation speed of 6000 rpm. PVC particles with diameter of 476 nm were used for calibration before every single measurement. After dilution 1:10 in ultrapure water, aliquots of 100 μL of P25, E171, P25@BSA and E171@BSA nanosols were injected in the disk of the centrifuge. Effective density values experimentally calculated from volumetric centrifugation measurements were used as input parameters for the size distribution calculations.

2.3.6. Asymmetric-flow field flow fractionation

The AF4 used for the separation of the unbound BSA from target NPs included an Eclipse Dualtec separation system (Wyatt Technology Europe GmbH, Dernbach, Germany) and an Agilent 1260 Infinity high-performance liquid chromatograph equipped with a degasser (G1322A), an isocratic pump (G1310B), an autosampler (G1329B) and a multi-wavelength detector (G1365C) set at $\lambda = 280$ nm, all from Agilent Technologies (Agilent Technologies, Santa Clara, USA). Regenerated cellulose (10 kDa) membranes were used in the Eclipse SC separation channel. The spacer height was 350 μm. The temperature of the channel was kept constant at 25 °C. The eluent was PBS (1x). Since the purpose of AF4 analysis was determining the concentration of free BSA, the fractionation of the sample was performed in such a way that BSA monomers and dimers were well resolved in the fractogram (high cross-flow), while the TiO_2 particles were washed out of the channel at the end of the run when setting the cross-flow to zero. The flow program and cross-flow settings are included in Table S1. The detector flow was set at 1.0 mL min^{-1}, the injection volume was 50 μL and the focus flow was 1.5 mL min^{-1}. The quantification of BSA was carried out by UV/VIS detector against a BSA-calibration curve (0–50 ppm). Calibration curves were generated for the BSA mono- and dimer. The correlation coefficient (R^2) was better than 0.99 in both cases. Prior to analysis, the membrane was conditioned injecting multiple times high concentrations of BSA, until the integrated monomer peak-area was constant. Samples were diluted 1:10 in PBS before analysis. P25@BSA and E171@BSA nanosols samples were analyzed by AF4. Each sample was analyzed three times and data were obtained by averaging the three measurements. For quality control purposes, BSA-suspensions of known concentration were injected. Recovery ranged from 97 to 103 %.

2.3.7. UV/VIS spectroscopy

P25@BSA and E171@BSA nanosols samples were centrifuged at 15 000 rpm for 10 min using Sorvall Legend XTR Centrifuge (Thermo Scientific), at the aim of separating particle-bound from unbound proteins [25]. The supernatant was analysed by UV/VIS spectroscopy using UV/VIS/NIR Spectometer Lambda 750 (PerkinElmer). The quantification of unbounded (free) BSA occurred exploiting the adsorption peak of at $\lambda = 280$ nm [26,27]. The BSA concentration in the supernatant was evaluated through a calibration curve obtained by plotting known BSA concentrations as a function of relative value of absorbance. The calibration curve showed correlation coefficients (R^2) above 0.99. Results from UV/VIS spectroscopy were reported as the average of three independent measurements.

2.3.8. Thermogravimetric analysis

Thermogravimetric analysis was performed on P25@BSA and E171@BSA nanosols, before and after centrifugation. In both cases, the samples were placed in an oven at low temperature (around 40 °C) for 24−48 hours to make sure they are completely dried. A Netzsch STA 449 F3 Jupiter® was used to run the TGA experiment by heating the dry sample to 800 °C, in air flux, at a rate of 10 °C/min. The weight of the sample was recorded as a function temperature. The weight loss data by TGA was used to quantify BSA adsorbed on TiO_2 NPs' surface, comparing the values of samples before and after centrifugation.

2.3.9. Circular dichroism

Circular dichroism spectra of BSA in the absence and in the presence of P25 and E171 NPs were recorded, on a Jasco J800 circular dichroism spectropolarimeter, in 5 mm path length cuvettes, 10 nm/min scan speed, averaged over 4 scans. Measurement range was from 260 to 190 nm and detector sensitivity was set to 200 millidegrees (mdeg). Initially, preliminary analyses were carried out on pristine P25 and E171 nanosols, in order to define the suitable samples' dilution for a good baseline. Pristine P25 and E171 nanosols were diluted 1:20 in ultrapure water and used as blank. CD analyses were performed on P25@BSA and E171@BSA nanosols diluted 1:10 in ultrapure water, before and after centrifugation, as well as supernatants and BSA solutions at the concentration used in colloidal heterocoagulation process (150 and 300 μg mL^{-1} in P25@BSA and E171@BSA, respectively). The characteristic dichroic signal of BSA was observed in the 190–200 nm spectral range with subtraction of the blank. The CD spectra were smoothed via a Savitsky–Golay model [28].

2.3.10. Specific surface area by BET method

Specific surface areas of SFD powders were measured by N_2 physisorption apparatus (Sorpty 1750 CE instruments) and single point by Brunauer-Emmett-Teller (BET) analysis method, in which samples were pre-treated under vacuum at 120 °C.

2.3.11. Field emission scanning electron microscopy

Morphological characterization of SFD powder was performed by scanning electronic microscopy analysis using a Carl Zeiss Sigma NTS microscope (Gmbh Öberkochen, Germany). The powder granules were fixed to aluminium stubs with conductive adhesive tape and sputter-metallized with gold. Qualitative analysis on size distribution was acquired by FESEM using ImageJ 1.52p software for more than 150 particles (National Institute of Health, USA).

2.3.12. X-ray photoelectron spectroscopy

Samples for XPS analyses were prepared using 10 μL aliquot, drop cast on cleaned Si wafer, obtained after centrifugation of suspensions, prepared dispersing a spatula of SFD powders in 1 mL of ultrapure water. The samples were dried under vacuum overnight. Before starting the XPS analysis, the Si wafers were mounted on a stainless steel sample-holder bar using a double side Cu UHV compatible tape and dried in a pre-chamber for 1.5 h in order to further dry and clean the samples. XPS measurements were performed in an Axis Ultra spectrometer (Kratos, Manchester, UK), using a Kα Al monochromatic source ($h\nu = 1486.6$ eV) operating at 150 W and X-ray spot-size of 400 × 700 μm^2 in hybrid mode. The residual pressure of the analysis chamber during the analysis was less than 8×10^{-9} Torr. For each sample, both survey spectra (0–1150 eV, pass energy 160 eV) and high-resolution spectra (pass energy at 20 eV) were recorded. Surface charge was stabilized compensated by a magnetic charge compensation system and the energy scale was calibrated by setting the C 1s hydrocarbon peak to 285.00 eV. The take-off angle for the acquisitions was 90° with respect to the sample surface. The spectrometer was calibrated following the standardized procedure [29]. The data were processed using Vision2 software (Kratos Analytical, UK) and the analysis of the XPS peaks was carried out using a commercial software package (Casa XPS2023, Casa Software Ltd., UK). Peak fitting was performed with no preliminary smoothing. Asymmetric Gaussian-Lorentian product functions were used to approximate the line shapes of the fitting components after a Tougaard-type background subtraction.

2.3.13. Fourier transform infrared spectroscopy-Attenuated total reflectance

FTIR-ATR was exploited to characterized the BSA shell on dry SFD powder samples, specifically to investigate any changes occurring on the secondary structure of BSA, estimating the α-helix, β-sheet, β –turn and random (unordered) contributions. The P25@BSA SFD and E171@BSA SFD, as well as P25 SFD and E171 SFD nanosols, and BSA alone, were pressed in dry form onto adhesive copper substrates forming thick (> 100 μm) and flat films. The measurements were performed in ATR mode, measured area was reduced via masking slits to 25 μm x 25 μm, acquired spectral range was 600-4000 cm^{-1}; spectral resolution used was 2.0 cm^{-1}; every spectrum was accumulated 258 times. The analyses were carried out using Bruker Hyperion μ-FTIR spectrometer with integrated microscope equipped with a combined 20x Cassegrain/ATR (Germanium crystal, diameter 100 μm, refractive index n = 4.0) objective. OPUS software (native Bruker data analysis environment) and OriginPro9.0 were used for data processing following the methodology described by Yang and colleagues [30].

3. Results and discussion

3.1. Preliminary characterization on pristine P25 and E171 samples

A preliminary characterization of pristine powder samples was performed. sp-ICPMS analysis of suspended P25 showed a monomodal particle size distribution with a most frequent size (mode, determined through Kernel density estimate) at 270 nm and the lower/upper bound at 200 nm and 400 nm respectively (Figure S2a). Otherwise, E171 presented a bimodal PSD, with the most frequent size of main peak at 280 nm and the second around 90 nm (Figure S2b). The size of pristine powder sample was also determined by FESEM and DLS techniques. FESEM image of P25 (Figure S2c) showed primary particles with a mean diameter of approximately 21 nm. This is confirmed also by the provider's product information sheet and literature [31]. Primary particles showed a strong tendency to form large agglomerates (about 600 nm), as confirmed by hydrodynamic diameters (d_{DLS}, Table 1). FESEM analysis of E171 sample showed the presence of primary particles larger than those found for P25 (Figure S2c,d), with a mean diameter around 90 nm as confirmed by sp-ICPMS (Figure S2b, second peak). On the other hand, the main peak at 280 nm observed in sp-ICPMS (Figure S2b) could be attributable to the size of agglomerates as demonstrated also by hydrodynamic diameter (d_{DLS} about 300 nm, Table 1). In literature [32,33], different E171 food grade TiO_2 NPs were analysed by sp-ICPMS and TEM analyses, pointing out a variability in the size of the primary particles, in a range between 20 nm and 250 nm. Summarizing the data collected by the different techniques, we could hypothesize that E171 have a lower tendency to form large agglomerates than P25. This could explain the greater consistency between data collected by different techniques (sp-ICPMS, FESEM and DLS) in E171 than P25.

XRD measurements showed that P25 is composed mainly by anatase with a not negligible amount of rutile phase, confirming the ratio 85 % anatase and 15 % rutile, indicated by provider and literature [31,34], while E171 is pure anatase [35]. XRD diffractograms are reported in Figure S3.

Table 1
Colloidal characterization results of samples diluted in ultrapure water.

	d_{DLS} [nm]	PDI	Z-pot_{ELS} [mV]	pH	$pH_{i.e.p.}$
E171	392.6 ± 2.3	0.2	−50.4 ± 5.9	6.2	2.8
P25	599.5 ± 49.8	0.5	+41.1 ± 2.3	3.7	5.9
BSA	916.1 ± 339.6	0.7	−17.7 ± 2.8	6.1	4.3
E171@BSA	517.5 ± 6.9	0.3	+2.8 ± 0.9	4.0	4.6
P25@BSA	2495 ± 538	0.5	−18.1 ± 2.7	5.4	4.3

3.2. Characterization of P25@BSA and E171@BSA nanosuspensions

A colloidal self-assembling method was chosen to promote BSA coating on TiO_2 surfaces, exploiting opposite charged nanoparticles [36]. In this regard, positively charged P25 NPs were mixed with BSA at its natural pH (about 6), where shows negative charge (pH isoelectric point of BSA around 4.5 [37–39]. On the other hand, positively charged BSA at acidic pH (around 3.5) was added to negatively charged E171 NPs. The negative charge of food grade TiO_2 is not unusual and the high negative zeta-potential is most likely due to the presence of a coating, such as phosphate groups [40,41]. The comparison of Z-pot vs pH curves results a very simple and rapid method to confirm the well-known interaction of BSA with a variety of natural and engineered surfaces, as a function of surface properties, BSA concentration and pH [42]. The first evidence of the occurred BSA coating derived by the observation of titration curves reported in Figs. 1a,b, showing the high correspondence found in TiO_2@BSA nanosuspensions and BSA curve that confirms the presence of BSA coating masking TiO_2 surfaces. In fact, in both cases, the TiO_2@BSA set upon the same isoelectric point of BSA (4.3), as was only BSA driving the acid/base behavior of TiO_2 coated surfaces (Table 1). The Z-pot and DLS-mean size curves vs amount of BSA added (Figs. 1c,d) allowed to make an estimation of the amount of BSA needed to completely coat the TiO_2 surface. This is only an empirical determination that identifies the beginning of Z-pot plateau with the minimum amount of capping agent required to mask the surface of the dispersed phase, as previously reported [43]. As can be observed, both size curves showed an abrupt increasing of dimension due to the addition of BSA that reverse the sign of Z-pot. After that the Z-pot slowly set upon a plateau, even if this is not so evident for both cases. The BSA amount identified in Figs. 1c,d (black circles) were added to TiO_2 to prepare the investigated TiO_2@BSA systems.

In order to be used as input parameters for CLS analysis, the effective densities of TiO_2 based nanosuspensions were experimentally measured by VCM method. Effective density (ρ^e_A) was calculated from V_{sed}, determined after centrifugation using Eq.1 (Table S2). The size distribution results obtained by CLS are reported in Fig. 2 and summarised in Table S2. The pristine P25 showed a mode around 540 nm, the introduction of BSA increasing it at about 1 μm (Fig. 3a). The pristine E171 showed a bimodal distribution with a main peak around 570 nm and a lower intensity peak at 1.16 μm. The modified E171@BSA nanosol showed a wide monomodal PSD with a diameter around 700 nm (Fig. 2b). The absorbance-based Stokes diameter results obtained by CLS are comparable with hydrodynamic diameter values measured by DLS technique (Table 1), whilst showed higher values if compared with sp-ICPMS analysis results.

All the techniques investigated revealed the presence of aggregated NPs with a bimodal distribution for pristine E171, nevertheless, the lack of correspondence between absolute values detected by CLS and sp-ICPMS is something not new, when techniques based on different physical principles are compared. Aggregates larger than 1 μm, in fact, highly impact on light scattering values, whilst have a negligible contribution on the total number of particles. Even if the transformation of absorbance based size distributions to number based distributions is very challenging in multi-component particle aggregates, the CLS derived number weighted distributions showed size values much more close to sp-ICPMS results, with modes of about 380 and 420 nm for the P25 and E171 pristine nanosol samples, respectively.

In general, there is a good reproducibility of CLS measured (absorbance based) distributions, as illustrated by two repetitive measurements for each sample and for each gradient considered, 0–8 % and 8–24 % (Fig. 2). The good match between size distributions determined with two different density gradients, suggests that the VCM method provides reasonably good effective density values for both the pristine and protein coated materials.

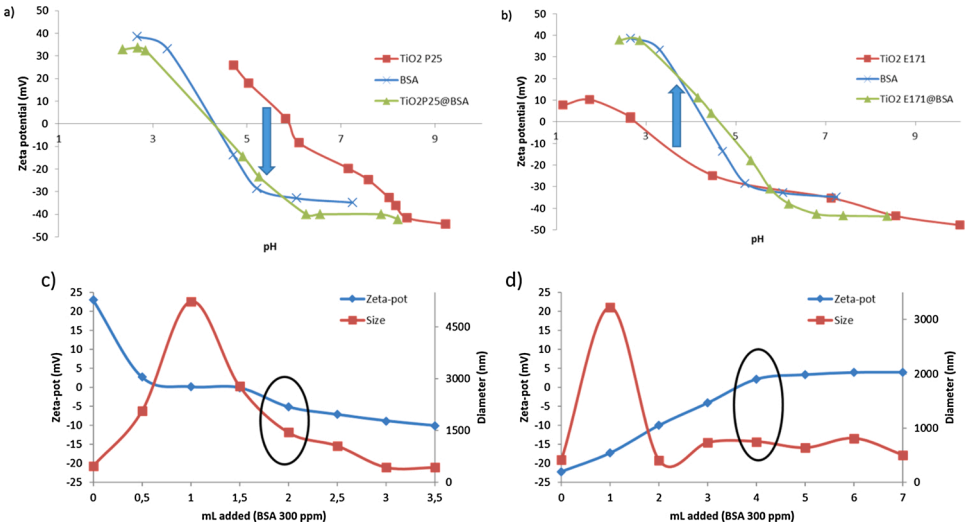

Fig. 1. Zeta-potential as a function of pH for a) P25-based and b) E171-based samples; zeta-potential and the size of BSA coated TiO_2 NPs as a function of BSA mL added to c) P25 and d) E171.

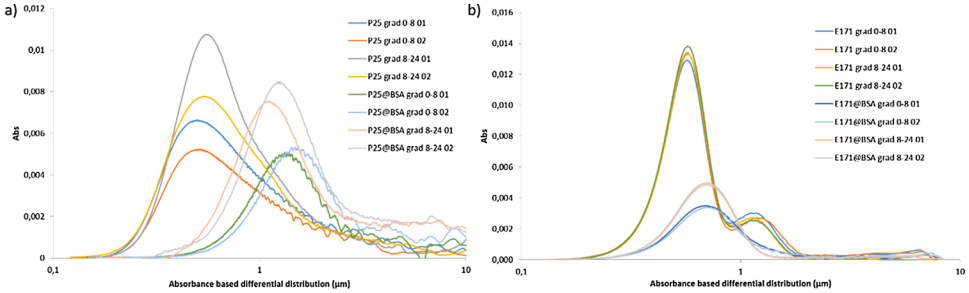

Fig. 2. Absorbance based PSD obtained by CLS method of a) P25 based nanosuspensions and b) E171 based nanosuspensions.

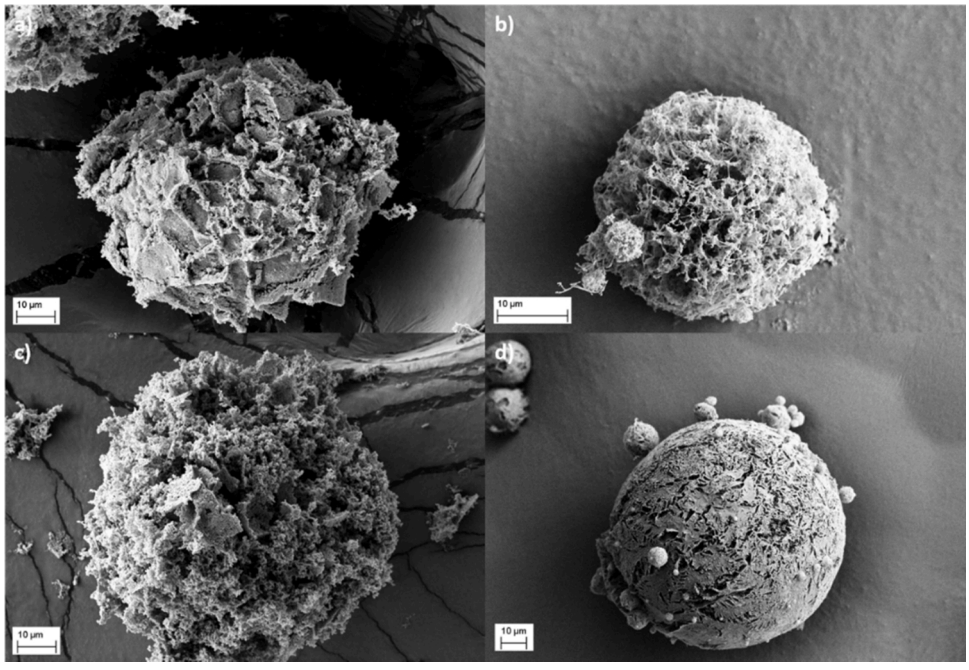

Fig. 3. FESEM images of a) P25 SFD, b) P25@BSA SFD, c) E171 SFD, d) E171@BSA SFD powders.

3.3. Characterization of SFD powders

Morphological characterization of powders obtained by spray-freeze-drying was performed using FESEM analysis. The relative images are reported in Figs. 3 and S4. P25 SFD sample (Figs. 3a) showed micrometric powder irregular in size and shape. The observed morphology suggests that the granules are characterized by very low mechanical strength. The addition of BSA improved the granulation process, in fact the sample P25@BSA SFD showed regular spherical granules (Fig. 3b). Moreover, the high magnification images (Figure S4a) showed a highly porous structure. A similar behaviour was observed for samples E171 SFD and E171@BSA SFD (Figs. 3c,d). The granules corresponding to pristine samples are irregular in size and shape, whilst BSA coated samples showed a more compact structure and a high porosity (Figures S4b). Quantitative analysis of FESEM images of SFD powders showed a wide size dimensional distribution, due to the limited control of spray-freeze-drying process (Figure S5).

Specific surface areas (SSA) of SFD powders were measured by BET method and the relative results are reported in Table S3, showing an increase of SSA for E171 samples, from 7 to 19 $m^2 g^{-1}$, most likely due to BSA dispersing action on pristine E171 particles.

XPS measurements allowed to calculate the atomic percentage of carbon, titanium, oxygen, nitrogen, phosphorous, sulphur and potassium (Table 2). A good correspondence between XPS data and BSA theoretical composition (% C 63.1; % N 16.8; % O 19.3; % S 0.8, excluding H not detectable by XPS) was found. The results relative to P25 SFD sample confirmed the presence of naked TiO_2 NPs with Ti:O ratio close to 1:2. The slightly higher amount of oxygen is due to surface contamination as illustrated in Figure S6, where the C1 s core level spectra of the samples are reported. On the other hand, the lower Ti:O ratio (0.364) together with the detection of additional elements, namely K and P in E171 SFD suggested the presence of a coating, most likely K-phosphorus compound. The detection of carbon in pristine P25 SFD and E171 SFD samples is attributable to contaminants mainly hydrocarbons, carbonyl and carboxyl moieties. Analysis of the Ti2p core level spectra showed the presence of a single doublet at 458.8 eV ($Ti2p_{3/2}$) with a spin-orbit splitting of 5.72 eV related to Ti^{4+} oxidation state (Figure S7) [44–47]. The core level O1 s spectra showed a major component related to the TiO_2 at about 530 eV and a minor component at about 531 eV attributable to organic moieties [C-O(R)] due to contamination (Figure S8). The presence of BSA coating was confirmed by the contribute of nitrogen observed both in P25@BSA SFD and E171@BSA SFD samples, due to the amino and amide groups abundant in BSA protein (Figure S9) and the corresponding decreases in Ti signal (Table 2) [13,48]. Moreover, the increase of carbon concentration and the difference in C1 s shape (Figure S6) further support the presence of BSA onto nanoparticles surfaces. The O1 s core level spectra also change drastically in the coated samples (Figure S8). In particular, the increase in intensity of the component at higher binding energy can be attributed to the presence of the protein coating. Moreover, the appearance of an additional component at about 533 eV attributable to aliphatic bonds further confirms the presence of the BSA coating [49]. Finally, the presence of sulphur can be attributed to the BSA, although very low amount was detected in E171@BSA SFD and total absence in P25@BSA SFD. Similarly, E.S. Bronze-Uhle and colleagues [50] demonstrated the presence of protein on TiO_2 P25 naked and superficially modified, after BSA adsorption. An interesting study useful as comparison with our results was reported by S. R. Sousa et al. [51], where human serum albumin (HSA) whose composition and behaviour are very similar to the BSA, was adsorbed onto commercial TiO_2. Through XPS analysis the adsorbed HAS was quantified. The kinetics of albumin adsorption on TiO_2 samples were followed by the C1 s peak intensity which increased with adsorption time. This was also observed following nitrogen N1 s that clearly increases due to HSA adsorption on TiO_2. The sulphur peak in S2p spectra was observed only at HAS high concentration (>0.3 mg/mL), confirming our finding. Considering the three dimensions of a BSA molecule (14 × 4 × 4 nm) and that the XPS analysis depth is about 10 nm, the results suggest BSA molecules are randomly adsorbed, both in flat and vertical orientation. Moreover, the large aggregation of NPs and their morphology do not exclude an inhomogeneous coverage of the NPs [13].

Table 2
Atomic percentages with relative standard deviations (St. Dev.) determined using XPS.

Sample	% C ± St. Dev.	% Ti ± St. Dev.	% O ± St. Dev.	% N ± St. Dev.	% P ± St. Dev.	% S ± St. Dev.	% K ± St. Dev.
P25 SFD	17.75 ± 1.06	26.40 ± 0.43	55.84 ± 0.66				
P25@BSA SFD*	49.79 ± 1.01	6.62 ± 0.74	29.32 ± 0.82	12.78 ± 0.64			
E171 SFD	11.76 ± 1.03	22.52 ± 0.70	61.86 ± 1.33		2.27 ± 0.76		1.59 ± 0.36
E171@BSA SFD	53.38 ± 1.08	5.08 ± 0.23	28.52 ± 0.49	12.69 ± 0.73		0.34 ± 0.41	
BSA	66.78 ± 0.72		18.41 ± 0.73	13.51 ± 0.50		0.50 ± 0.08	
BSA (theory)	63.1		19.3	16.8		0.8	

* In this sample was detected also 1.5 % Si due to the contribute to Si wafer support.

3.4. Quantitative determination of bound BSA

The quantification of free and bound BSA in P25@BSA and E171@BSA nanosols represents a challenging objective of the proposed self-assembling BSA coating strategy, so we deeply investigated through an orthogonal multi-techniques approach. Ultra-centrifugation coupled with UV/VIS spectroscopy, was exploited to quantify the concentration of unbound BSA. The results revealed a high amount of free BSA, remaining in the surnatant after centrifugation (Table 3). These results are explained by the presence of an excess of BSA. If reported to specific surface area, in fact, the two systems present a total amount of BSA equal to around 3 mg/m^2 for both P25 and E171 samples, respectively, in agree with the adsorbed amount (1.31 ± 0.2 mg/m^2 at pH 5), measured in literature [52]. Thermogravimetric analyses (Figure S10) performed on P25@BSA and E171@BSA, before and after ultra-centrifugation (P25@BSA UC and E171@BSA UC samples), confirmed such results. The presence of BSA excess in heterocoagulated TiO_2@BSA nanosols, is confirmed by the reduction of adsorbed BSA calculated by TGA that passes from 87.1 and 5.2 mg/m^2 of nominal concentration to 14.8 and 3.7 mg/m^2 for TiO_2 P25 and E171, respectively. The trend was clearly confirmed if expressing the amount of BSA adsorbed as molecules/cm^2. In fact, very high values were calculated for E171@BSA and P25@BSA samples, passing from 1.68 × 10^{13} and 3.87 × 10^{12} molecules/cm^2, before centrifugation, to 2.23 × 10^{12} and 2.81 × 10^{12} molecules/cm^2 for E171@BSA UC and P25@BSA UC, respectively (Table S4).

These data confirm that the amount of BSA needed to cover the surface, as derived by Z-pot titrations of Figs. 1c,d, is overestimated. In fact, the amount of adsorbed BSA, calculated by subtracting the amount

Table 3
Adsorbed BSA (mg m^{-2}) as calculated by ultra-centrifugation (UC) coupled with UV/VIS spectroscopy and TGA techniques, compared with AF4 separation technique coupled with UV/VIS detector.

	UC-UV/VIS	AF4*-UV/VIS	UC-TGA
E171@BSA	11.0 ± 3.8	3.7 ± 0.3	14.8
P25@BSA	3.2 ± 0.2	2.4 ± 0.1	3.7

* Quantification against monomer peak.

of free BSA from the total nominal concentration, confirmed that the value adsorbed (few units expressed as mg/m^2 of TiO_2 surface) is in line with literature data [53,54] and is comparable between samples and techniques used for its estimation. If normalised for the total amount of surface area exposed, the BSA covering E171 resulted even higher than that covering P25, as negative charge and most likely more hydrophilic E171 surface, promoted the adsorption of protein. In addition, for both samples, the lower amount of BSA adsorbed and measured by AF4, is most likely due to the higher amount of BSA that is forced to precipitate on TiO_2 surface, during ultracentrifugation steps associated to UV/VIS and TG analysis. In literature several studies quantifying the amount of BSA adsorbed on nano-TiO_2 are reported and present similar results. The amount of BSA adsorbed on commercial TiO_2 and measured by SPR (Surface Plasmon Resonance) resulted 4,3 mg/m^2 [55]. Márquez and colleagues [56] determined the number of adsorbed BSA molecules on TiO2 (P25) agglomerates through TG analysis. The data indicated the presence of 2.1×10^{13}, 3.8×10^{13} and 4.5×10^{13} BSA molecules adsorbed per TiO_2 for samples prepared with a [BSA]/[TiO2] ratio in a similar range we used, equal to 0.1, 0.2 and 0.4, respectively. An interesting study [57] investigated the adsorption of different types of blood proteins on anatase TiO_2 NPs, confirming the high affinity of nano-TiO_2 surfaces for BSA similar proteins (HAS, γ-globulins, and fibrinogen).

CD measurements of P25@BSA and E171@BSA nanosols (before and after centrifugation) as well as supernatants and free BSA solutions were used to qualitative assess binding of BSA to TiO_2 NP surface. The CD spectrum of free BSA is characterized by the presence of two negative bands at 209 and 222 nm, typical of a mainly alpha-helical protein [58]. We observed that the intensity of the negative bands changed without any discernible change in the spectra profile. In particular, we observed the presence of high amounts of unbound BSA and barely discernible spectra for bound BSA (spectra E171@BSA UC and P25@BSA UC in Figure S11) that indicated low amounts of BSA bound to nanoparticles and prevented a more quantitative analysis.

Summarising, the multi-techniques approach proposed to determine the bound and unbound BSA in TiO_2@BSA nanosols, was successfully applied and allowed to optimize the proposed design strategy that can be applied also to other nanoparticles, once verified the presence and amount of BSA needed to cover the exposed surface. In fact, the various methods used lead to results that are consistent with each other, providing a platform for the reciprocal validation of the methodologies used to characterise protein (more general organic) coatings on inorganic nanoparticles. Briefly, the main results obtained can be summarized, as follows. P25@BSA sample showed a substantial BSA weight % loss, but still less than 50 %. On the other hand, E171@BSA sample showed very high BSA loss (>90 %), due to the presence of a negative coating on pristine E171 NPs.

In order to prove the presence of a BSA coating, after removing the unbound BSA fraction, Z-pot as a function of pH titrations were performed on P25@BSA UC and E171@BSA UC. Figure S12 shows a certain similarity with the curves, reported in Fig. 1a,b, relative to the sample before centrifugation. In fact, also in the Figure S12, we can observe the high correspondence found in TiO_2@BSA UC samples and BSA guaranteeing the presence of BSA on TiO_2 NPs' surfaces. Both TiO_2@BSA UC samples, after centrifugation, showed an isoelectric point consistent with that of BSA (4.3), demonstrating that despite the low amounts of BSA present in ultracentrifuged samples, the covering of the surfaces of TiO_2 NPs was insured. This confirmed once again that BSA quantities in TiO_2@BSA nanosols were added in excess.

3.5. BSA secondary structure determination by FTIR-ATR

FTIR-ATR analyses were carried out on powder SFD samples for determining the secondary structure of BSA. In the specific, the amide I band deconvolution was exploited to quantify the secondary structural composition, according to the method described by Yang and colleagues [30]. First of all, a basic peaks assignment was performed on FTIR ATR spectrum of E171@BSA SFD sample (Figure S13). Spectrum of P25@BSA SFD sample (not reported) exhibits similar features. Then further data processing was made for the protein secondary structure analysis through Amide I (AmI) band deconvolution. From Figure S13, contributions from TiO_2, protein backbone and protein side chains can be observed and assigned [59]. Detailed description of method used to extrapolate the secondary structure composition is reported in ESI. Fig. 4 show the AmI band deconvolution and subsequent bound protein secondary structure analysis for P25@BSA SFD sample as example. Spectrum of E171@BSA SFD sample (not reported) exhibits similar features. Quantitative estimation of protein secondary structure was based on the assumption that protein can be considered as a linear sum of the definite fundamental secondary structural elements: α-helix, ß-sheet, ß-turn and random (or unordered) [60].

The data relative to the secondary structure composition of BSA adsorbed on TiO_2 are summarised in Table 4. The main secondary structure of free BSA, α-helix, is reported to be around 60–65 % of the total secondary content, as confirmed by our data. However, literature data give values that vary by around 10 % [61–66]. Comparing bound and free BSA data (Δ), we consider a secondary structural content change greater than 10 % significant. The changes indicate that the protein was unfolding and/or denaturing on the surface. As demonstrated by [55] the change of protein structure indicates the particles and BSA interactions took place. The increase of the β-sheet and unordered conformations contents on the expense of the α-helix content indicates conformational changes of BSA protein. Indeed, the loss of α-helix structure is expected to be balanced by an increase in β-structures [67]. These changes are due to the formation of BSA shell on TiO_2 NPs, ensuring the presence of biocompatible coating on our target TiO_2. The BSA-coating is here proposed as safe-by-design strategy to uniform the surface reactivity and let NPs exposing the same biocompatible surface NPs. For BSA on P25 strong interactions with TiO_2 surface was confirmed by significant conformational change (>10 %). This led to a great denaturation effect of BSA on TiO_2 surface that may be a result of stronger electrostatic interactions between BSA and hydroxyl groups on TiO_2 surface. On the other hand, just a slight conformational change corresponding with weak interactions between BSA and TiO_2 surfaces was estimated for E171@BSA SFD sample. These finds are consistent with data relative to quantitative determination of unbound BSA.

4. Conclusions

The characterisation and estimation of protein adsorption on NPs surface is a key step for the comprehension of mechanism that drive nano-bio interactions, but can also support the validation of potentially safe-by-design solution for producing and using less hazardous NPs. In order to turn the idea of BSA coating in a sustainable safe-by-design strategy, we looked for a self-assembling and easily scalable colloidal approach and implemented an orthogonal multi-technique characterization platform to characterise and assess the amount of BSA adsorbed on two different TiO_2 NPs (well-known P25 and food grade E171). We used an heterocoagulation colloidal approach and play with surface charges to promote the interaction between TiO_2 surfaces (P25 and E171) and BSA. Different techniques were used to characterise BSA adsorbed on TiO_2 surfaces and all supported the presence of BSA coating, masking TiO_2 surface. What was interesting to note is that the three techniques (AF4, UV/VIS and TGA) provided comparable results and showed only a 10 % of initially added BSA, binding TiO_2 E171 surface, whilst a higher percentage (around 60 %), binding TiO_2 P25 surface. Nevertheless, if BSA amount is normalised for surface area exposed, the amount covering E171 resulted higher than P25, as negative charge and most likely more hydrophilic E171 surface, promoted the adsorption of albumin. Overall, the implemented orthogonal multi-techniques platform improved knowledge on TiO_2@BSA nanocomposite system that represent a simple model for nano-biocorona, but also a

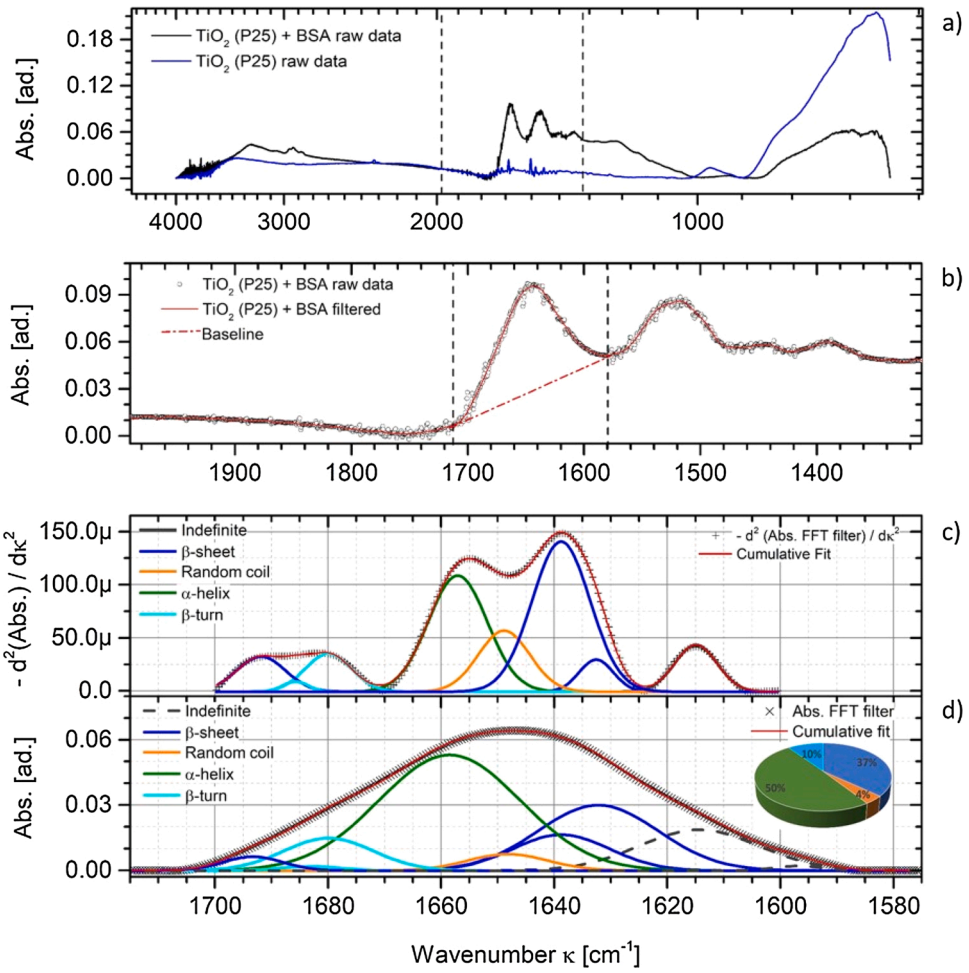

Fig. 4. a) FTIR-ATR spectrum of P25@BSA SFD sample; b) interest region, peak assignment, FFT smoothing and baseline for Amide I peak; c) second derivate analysis (SDA) of FFT filtered; d) adsorbed protein structural composition obtained by AmI band deconvolution according to constrains from SDA using Gaussian peaks.

Table 4
Secondary structure composition of BSA determined via curve fitting for BSA free and bound to TiO_2 nanoparticle surfaces.

	BSA	E171@BSA SFD (Δ)*	P25@BSA SFD (Δ)*
α-helix	0.65	0.50 (-0.15)	0.42 (-0.23)
β-sheet	0.26	0.37 (+0.11)	0.46 (+0.20)
Random coil	0.04	0.03 (-0.01)	0.05 (+0.01)
β-turn	0.05	0.10 (+0.05)	0.07 (+0.02)

Average Standard deviation ≈ 2%.
* Δ = difference between bound and free BSA secondary structure content.

potential safe-by-design strategy to intentionally control and level-off nanoparticles surface chemistry and reactivity.

CRediT authorship contribution statement

Simona Ortelli: Conceptualization, Methodology, Investigation, Data curation, Writing - original draft, Writing - review & editing. **Anna L. Costa:** Conceptualization, Writing - review & editing, Supervision, Funding acquisition. **Ilaria Zanoni:** Methodology, Investigation, Data curation, Writing - review & editing. **Magda Blosi:** Conceptualization, Writing - review & editing. **Otmar Geiss:** Methodology, Investigation, Data curation, Writing - review & editing. **Ivana Bianchi:** Methodology, Investigation, Data curation. **Dora Mehn:** Methodology, Investigation, Data curation, Writing - review & editing. **Francesco Fumagalli:** Methodology, Investigation, Data curation, Writing - review & editing. **Giacomo Ceccone:** Methodology, Investigation, Data curation, Writing - review & editing. **Giuditta Guerrini:** Methodology, Data curation. **Luigi Calzolai:** Conceptualization, Data curation, Writing - review & editing, Supervision.

Declaration of Competing Interest

The authors report no declarations of interest.

Acknowledgements

This work was supported by Joint Research Centre (JRC) of the European Commission in accordance with the Research Infrastructure Access Agreement N°335559/6 2019-1-RD–Nanobiotech within the "Open access to JRC Research Infrastructures" programme. The European project PATROLS (H2020-NMBP-29-2017, number 760813) is also acknowledged for financial support.

Appendix A. Supplementary data

Supplementary material related to this article can be found, in the online version, at doi:https://doi.org/10.1016/j.colsurfb.2021.112037.

References

[1] X. Gao, G.V. Lowry, Progress towards standardized and validated characterizations for measuring physicochemical properties of manufactured nanomaterials relevant to nano health and safety risks, NanoImpact. 9 (2018) 14–30, https://doi.org/10.1016/j.impact.2017.09.002.

[2] A.E. Nel, L. Mädler, D. Velegol, T. Xia, E.M.V. Hoek, P. Somasundaran, F. Klaessig, V. Castranova, M. Thompson, Understanding biophysicochemical interactions at the nano–bio interface, Nat. Mater. 8 (2009) 543–557, https://doi.org/10.1038/nmat2442.

[3] I. Lynch, K.A. Dawson, Protein-nanoparticle interactions, Nano Today 3 (2008) 40–47, https://doi.org/10.1016/S1748-0132(08)70014-8.

[4] M.P. Monopoli, C. Aberg, A. Salvati, K.A. Dawson, Biomolecular coronas provide the biological identity of nanosized materials, Nat. Nanotechnol. 7 (2012) 779–786, https://doi.org/10.1038/nnano.2012.207.

[5] M.P. Monopoli, F.B. Bombelli, K.A. Dawson, Nanoparticle coronas take shape, Nat. Nanotechnol. 6 (2011) 11–12, https://doi.org/10.1038/nnano.2010.267.

[6] V.H. Nguyen, B.-J. Lee, Protein corona: a new approach for nanomedicine design, Int. J. Nanomedicine 12 (2017) 3137–3151, https://doi.org/10.2147/IJN.S129300.

[7] J.B. Ferrado, A.A. Perez, F.F. Visentini, G.A. Islan, G.R. Castro, L.G. Santiago, Formation and characterization of self-assembled bovine serum albumin nanoparticles as chrysin delivery systems, Colloids Surf. B Biointerfaces 173 (2019) 43–51, https://doi.org/10.1016/j.colsurfb.2018.09.046.

[8] K. Bolaños, M.J. Kogan, E. Araya, Capping gold nanoparticles with albumin to improve their biomedical properties, Int. J. Nanomedicine 14 (2019) 6387–6406, https://doi.org/10.2147/IJN.S210992.

[9] B. Elsadek, F. Kratz, Impact of albumin on drug delivery–new applications on the horizon, J. Control. Release 157 (2012) 4–28, https://doi.org/10.1016/j.jconrel.2011.09.069.

[10] F. Kratz, Albumin as a drug carrier: design of prodrugs, drug conjugates and nanoparticles, J. Control. Release 132 (2008) 171–183, https://doi.org/10.1016/j.jconrel.2008.05.010.

[11] G. Be, X. Z, F. J, G. Vh, Bovine serum albumin adsorption on SiO2 and TiO2 nanoparticle surfaces at circumneutral and acidic pH: a tale of two nano-bio surface interactions, J. Colloid Interface Sci. 493 (2017) 334–341, https://doi.org/10.1016/j.jcis.2017.01.011.

[12] R.R. Kudarha, K.K. Sawant, Albumin based versatile multifunctional nanocarriers for cancer therapy: fabrication, surface modification, multimodal therapeutics and imaging approaches, Mater. Sci. Eng. C 81 (2017) 607–626, https://doi.org/10.1016/j.msec.2017.08.004.

[13] Z. Huang, T. Gengenbach, J. Tian, W. Shen, G. Garnier, Effect of bovine serum albumin treatment on the aging and activity of antibodies in paper diagnostics, Front. Chem. 6 (2018) 161, https://doi.org/10.3389/fchem.2018.00161.

[14] E. Mansfield, K.M. Tyner, C.M. Poling, J.L. Blacklock, Determination of nanoparticle surface coatings and nanoparticle purity using microscale thermogravimetric analysis, Anal. Chem. 86 (2014) 1478–1484, https://doi.org/10.1021/ac402888v.

[15] D.R. Baer, The Chameleon effect: characterization challenges due to the variability of nanoparticles and their surfaces, Front. Chem. 6 (2018), https://doi.org/10.3389/fchem.2018.00145.

[16] S. Mourdikoudis, R.M. Pallares, N.T.K. Thanh, Characterization techniques for nanoparticles: comparison and complementarity upon studying nanoparticle properties, Nanoscale. 10 (2018) 12871–12934, https://doi.org/10.1039/C8NR02278J.

[17] S. Soares, J. Sousa, A. Pais, C. Vitorino, Nanomedicine: principles, properties, and regulatory issues, Front. Chem. 6 (2018), https://doi.org/10.3389/fchem.2018.00360.

[18] M. Younes, G. Aquilina, L. Castle, K.-H. Engel, P. Fowler, M.J.F. Fernandez, P. Fürst, U. Gundert-Remy, R. Gürtler, T. Husøy, M. Manco, W. Mennes, P. Moldeus, S. Passamonti, R. Shah, I. Waalkens-Berendsen, D. Wölfle, E. Corsini, F. Cubadda, D.D. Groot, R. FitzGerald, S. Gunnare, A.C. Gutleb, J. Mast, A. Mortensen, A. Oomen, A. Piersma, V. Plichta, B. Ulbrich, H.V. Loveren, D. Benford, M. Bignami, C. Bolognesi, R. Crebelli, M. Dusinska, F. Marcon, E. Nielsen, J. Schlatter, C. Vleminckx, S. Barmaz, M. Carfí, C. Civitella, A. Giarola, A.M. Rincon, R. Serafimova, C. Smeraldi, J. Tarazona, A. Tard, M. Wright, Safety assessment of titanium dioxide (E171) as a food additive, Efsa J. 19 (2021) e06585, https://doi.org/10.2903/j.efsa.2021.6585.

[19] H. Wu, L. Huang, A. Rose, V.H. Grassian, Impact of surface adsorbed biologically and environmentally relevant coatings on TiO 2 nanoparticle reactivity, Environ. Sci. Nano 7 (2020) 3783–3793, https://doi.org/10.1039/D0EN00706D.

[20] A. Precupas, D. Gheorghe, A. Botea-Petcu, A.R. Leonties, R. Sandu, V.T. Popa, E. Mariussen, E.Y. Naouale, E. Rundén-Pran, V. Dumit, Y. Xue, M.R. Cimpan, M. Dusinska, A. Haase, S. Tanasescu, Thermodynamic parameters at bio–nano interface and nanomaterial toxicity: a case study on BSA interaction with ZnO, SiO2, and TiO2, Chem. Res. Toxicol. (2020), https://doi.org/10.1021/acs.chemrestox.9b00468.

[21] A. Lolli, M. Blosi, S. Ortelli, A.L. Costa, I. Zanoni, D. Bonincontro, F. Carella, S. Albonetti, Innovative synthesis of nanostructured composite materials by a spray-freeze drying process: efficient catalysts and photocatalysts preparation, Catal. Today 334 (2019) 193–202, https://doi.org/10.1016/j.cattod.2018.11.022.

[22] ISO/TS 19590:2017, ISO, 2020 (Accessed July 8, 2020), https://www.iso.org/cms/render/live/en/sites/isoorg/contents/data/standard/06/54/65419.html.

[23] H.E. Pace, N.J. Rogers, C. Jarolimek, V.A. Coleman, C.P. Higgins, J.F. Ranville, Determining transport efficiency for the purpose of counting and sizing nanoparticles via single particle inductively coupled plasma mass spectrometry, Anal. Chem. 83 (2011) 9361–9369, https://doi.org/10.1021/ac201952t.

[24] C. Song, P. Wang, H.A. Makse, A phase diagram for jammed matter, Nature. 453 (2008) 629–632, https://doi.org/10.1038/nature06981.

[25] T. Cedervall, I. Lynch, S. Lindman, T. Berggård, E. Thulin, H. Nilsson, K.A. Dawson, S. Linse, Understanding the nanoparticle-protein corona using methods to quantify exchange rates and affinities of proteins for nanoparticles, Proc. Natl. Acad. Sci. U. S.A. 104 (2007) 2050–2055, https://doi.org/10.1073/pnas.0608582104.

[26] P. Huang, Z. Li, H. Hu, D. Cui, Synthesis and characterization of bovine serum albumin-conjugated copper sulfide nanocomposites, J. Nanomater. 2010 (2010) e641545, https://doi.org/10.1155/2010/641545.

[27] F. Jernström, Self-assembled monolayers of alkanethiols: A study of surface composition, wettability, and adsorption of proteins and peptides, (n.d.) 41.

[28] Abraham Savitzky, M.J.E. Golay, Smoothing and differentiation of data by simplified least squares procedures, Anal. Chem. 36 (1964) 1627–1639, https://doi.org/10.1021/ac60214a047.

[29] ISO 15472:2010(en), Surface Chemical Analysis — X-ray Photoelectron Spectrometers — Calibration of Energy Scales, 2020. https://www.iso.org/obp/ui/#iso:std:iso:15472:ed-2:v1:en.

[30] H. Yang, S. Yang, J. Kong, A. Dong, S. Yu, Obtaining information about protein secondary structures in aqueous solution using Fourier transform IR spectroscopy, Nat. Protoc. 10 (2015) 382–396, https://doi.org/10.1038/nprot.2015.024.

[31] H. Jensen, J.H. Pedersen, J.E. J∅rgensen, J.S. Pedersen, K.D. Joensen, S.B. Iversen, E.G. S∅gaard, Determination of size distributions in nanosized powders by TEM, XRD, and SAXS, J. Exp. Nanosci. 1 (2006) 355–373, https://doi.org/10.1080/17458080600752482.

[32] G. Bucher, F. Auger, Combination of 47Ti and 48Ti for the determination of highly polydisperse TiO2 particle size distributions by spICP-MS, J. Anal. At. Spectrom. 34 (2019) 1380–1386, https://doi.org/10.1039/C9JA00101H.

[33] O. Geiss, J. Ponti, C. Senaldi, I. Bianchi, D. Mehn, J. Barrero, D. Gilliland, R. Matissek, E. Anklam, Characterisation of food grade titania with respect to nanoparticle content in pristine additives and in their related food products, Food Addit. Contam. Part A 37 (2020) 239–253, https://doi.org/10.1080/19440049.2019.1695067.

[34] S. Bakardjieva, J. Šubrt, V. Štengl, M.J. Dianez, M.J. Sayagues, Photoactivity of anatase–rutile TiO2 nanocrystalline mixtures obtained by heat treatment of homogeneously precipitated anatase, Appl. Catal. B 58 (2005) 193–202, https://doi.org/10.1016/j.apcatb.2004.06.019.

[35] M. Dorier, D. Béal, C. Marie-Desvergne, M. Dubosson, F. Barreau, E. Houdeau, N. Herlin-Boime, M. Carriere, Continuous in vitro exposure of intestinal epithelial cells to E171 food additive causes oxidative stress, inducing oxidation of DNA bases but no endoplasmic reticulum stress, Nanotoxicology. 11 (2017) 751–761, https://doi.org/10.1080/17435390.2017.1349203.

[36] S. Ortelli, A.L. Costa, Nanoencapsulation techniques as a “safer by (molecular) design” tool, Nano-structures Nano-objects 13 (2018) 155–162, https://doi.org/10.1016/j.nanoso.2016.03.006.

[37] A.K. Bajpai, Adsorption of bovine serum albumin onto glass powder surfaces coated with polyvinyl alcohol, J. Appl. Polym. Sci. 78 (2000) 933–940, https://doi.org/10.1002/1097-4628(20001031)78:5<933::AID-APP10>3.0.CO;2-G.

[38] T. Kopac, K. Bozgeyik, J. Yener, Effect of pH and temperature on the adsorption of bovine serum albumin onto titanium dioxide, Colloids Surf. A Physicochem. Eng. Asp. 322 (2008) 19–28, https://doi.org/10.1016/j.colsurfa.2008.02.010.

[39] S. Servagent-Noinville, M. Revault, H. Quiquampoix, M. Baron, Conformational changes of bovine serum albumin induced by adsorption on different clay surfaces: FTIR analysis, J. Colloid Interface Sci. 221 (2000) 273–283, https://doi.org/10.1006/jcis.1999.6576.

[40] J.-S. Hwang, J. Yu, H.-M. Kim, J.-M. Oh, S.-J. Choi, Food additive titanium dioxide and its fate in commercial foods, Nanomaterials Basel (Basel) 9 (2019), https://doi.org/10.3390/nano9081175.

[41] M. Janus, Application of Titanium Dioxide, 2017, https://doi.org/10.5772/intechopen.70121.

[42] H.T.M. Phan, S. Bartelt-Hunt, K.B. Rodenhausen, M. Schubert, J.C. Bartz, Investigation of Bovine Serum Albumin (BSA) Attachment onto Self-Assembled Monolayers (SAMs) Using Combinatorial Quartz Crystal Microbalance with Dissipation (QCM-D) and Spectroscopic Ellipsometry (SE), PLoS One 10 (2015), e0141282, https://doi.org/10.1371/journal.pone.0141282.

[43] A.L. Costa, C. Galassi, R. Greenwood, alpha-Alumina-H2O interface analysis by electroacoustic measurements, J. Colloid Interface Sci. 212 (1999) 350–356, https://doi.org/10.1006/jcis.1998.6070.

[44] S. Benkoula, O. Sublemontier, M. Patanen, C. Nicolas, F. Sirotti, A. Naitabdi, F. Gaie-Levrel, E. Antonsson, D. Aureau, F.-X. Ouf, S.-I. Wada, A. Etcheberry, K. Ueda, C. Miron, Water adsorption on TiO 2 surfaces probed by soft X-ray spectroscopies: bulk materials vs. Isolated nanoparticles, Sci. Rep. 5 (2015) 15088, https://doi.org/10.1038/srep15088.

[45] J.T. Mayer, U. Diebold, T.E. Madey, E. Garfunkel, Titanium and reduced titania overlayers on titanium dioxide(110), J. Electron Spectros. Relat. Phenomena 73 (1995) 1–11, https://doi.org/10.1016/0368-2048(94)02258-5.

[46] K. Rasmussen, J. Mast, P.-J. De Temmerman, E. Verleysen, N. Waegeneers, F. Van Steen, J.C. Pizzolon, L. De Temmerman, E. Van Doren, K.A. Jensen, R. Birkedal, M. Levin, S.H. Nielsen, I.K. Koponen, P.A. Clausen, V. Kofoed-Sørensen, Y. Kembouche, N. Thieriet, O. Spalla, C. Giuot, D. Rousset, O. Witschger, S. Bau, B. Bianchi, C. Motzkus, B. Shivachev, L. Dimowa, R. Nikolova, D. Nihtianova, M. Tarassov, O. Petrov, S. Bakardjieva, D. Gilliland, F. Pianella, G. Ceccone, V. Spampinato, G. Cotogno, P. Gibson, C. Gaillard, A. Mech, Titanium Dioxide, NM-100, NM-101, NM-102, NM-103, NM-104, NM-105: Characterisation and Physico-Chemical Properties, Publications Office of the European Union, 2014

(accessed July 29, 2020), https://publications.jrc.ec.europa.eu/repository/handle/111111111/31713.
[47] Z. Wang, S. Liu, X. Cao, S. Wu, C. Liu, G. Li, W. Jiang, H. Wang, N. Wang, W. Ding, Preparation and characterization of TiO2 nanoparticles by two different precipitation methods, Ceram. Int. 46 (2020) 15333–15341, https://doi.org/10.1016/j.ceramint.2020.03.075.
[48] R.N. Foster, E.T. Harrison, D.G. Castner, ToF-SIMS and XPS characterization of protein films adsorbed onto bare and sodium styrenesulfonate-grafted gold substrates, Langmuir. 32 (2016) 3207–3216, https://doi.org/10.1021/acs.langmuir.5b04743.
[49] Surface Analysis of Polymers by X.P.S. and Static SIMS, (n.d.). https://www.cambridge.org/core/books/surface-analysis-of-polymers-by-xps-and-static-sims/C2008EFA035292E66F8786BC31572110 (accessed November 26, 2020).
[50] E.S. Bronze-Uhle, L.F.G. Dias, L.D. Trino, A.A. Matos, R.C. de Oliveira, P.N. Lisboa-Filho, Physicochemical characterization of albumin immobilized on different TiO2 surfaces for use in implant materials, Colloids Surf. A Physicochem. Eng. Asp. 564 (2019) 39–50, https://doi.org/10.1016/j.colsurfa.2018.12.028.
[51] S.R. Sousa, P. Moradas-Ferreira, B. Saramago, L.V. Melo, M.A. Barbosa, Human serum albumin adsorption on TiO2 from single protein solutions and from plasma, Langmuir. 20 (2004) 9745–9754, https://doi.org/10.1021/la049158d.
[52] D.T. Wassell, G. Embery, Adsorption of bovine serum albumin on to titanium powder, Biomaterials. 17 (1996) 859–864, https://doi.org/10.1016/0142-9612(96)83280-7.
[53] B.E. Givens, Z. Xu, J. Fiegel, V.H. Grassian, Bovine serum albumin adsorption on SiO2 and TiO2 nanoparticle surfaces at circumneutral and acidic pH: a tale of two nano-bio surface interactions, J. Colloid Interface Sci. 493 (2017) 334–341, https://doi.org/10.1016/j.jcis.2017.01.011.
[54] Bovine Serum Albumin Adsorption on TiO2 Nanoparticle Surfaces: Effects of pH and Coadsorption of Phosphate on Protein–Surface Interactions and Protein Structure | The Journal of Physical Chemistry C, (n.d.). https://pubs.acs.org/doi/abs/10.1021/acs.jpcc.7b07525 (accessed June 29, 2021).
[55] M. Bukackova, R. Marsalek, Interaction of BSA with ZnO, TiO2, and CeO2 nanoparticles, Biophys. Chem. 267 (2020), 106475, https://doi.org/10.1016/j.bpc.2020.106475.
[56] A. Márquez, T. Berger, A. Feinle, N. Hüsing, M. Himly, A. Duschl, O. Diwald, Bovine serum albumin adsorption on TiO2 colloids: the effect of particle agglomeration and surface composition, Langmuir. 33 (2017) 2551–2558, https://doi.org/10.1021/acs.langmuir.6b03785.
[57] P. Høl, Z. Ekeland Allouni, N.R. Gjerdet, M.R. Cimpan, The Effect of Blood Protein Adsorption on Cellular Uptake of Anatase TiO2 Nanoparticles, IJN, 2015, p. 687, https://doi.org/10.2147/IJN.S72726.
[58] N.J. Greenfield, Applications of circular dichroism in protein and peptide analysis, Trac Trends Anal. Chem. 18 (1999) 236–244, https://doi.org/10.1016/S0165-9936(98)00112-5.
[59] M.H. Vos, Ultrafast dynamics of ligands within heme proteins, Biochimica et Biophysica Acta (BBA) - Bioenergetics 1777 (2008) 15–31, https://doi.org/10.1016/j.bbabio.2007.10.004.
[60] J. Kong, S. Yu, Fourier transform infrared spectroscopic analysis of protein secondary structures, Acta Biochim. Biophys. Sin. (Shanghai) 39 (2007) 549–559, https://doi.org/10.1111/j.1745-7270.2007.00320.x.
[61] A. Bouhekka, T. Bürgi, In situ ATR-IR spectroscopy study of adsorbed protein: visible light denaturation of bovine serum albumin on TiO2, Appl. Surf. Sci. 261 (2012) 369–374, https://doi.org/10.1016/j.apsusc.2012.08.017.
[62] F. Friedrichs, All about albumin. biochemistry, genetics, and medical applications, Food / Nahrung. 41 (1997), https://doi.org/10.1002/food.19970410631, 382–382.
[63] İ. Gülseren, D. Güzey, B.D. Bruce, J. Weiss, Structural and functional changes in ultrasonicated bovine serum albumin solutions, Ultrason. Sonochem. 14 (2007) 173–183, https://doi.org/10.1016/j.ultsonch.2005.07.006.
[64] B. Jachimska, A. Pajor, Physico-chemical characterization of bovine serum albumin in solution and as deposited on surfaces, Bioelectrochemistry. 87 (2012) 138–146, https://doi.org/10.1016/j.bioelechem.2011.09.004.
[65] K. Murayama, Y. Wu, B. Czarnik-Matusewicz, Y. Ozaki, Two-Dimensional/Attenuated total reflection infrared correlation spectroscopy studies on secondary structural changes in human serum albumin in aqueous solutions: pH-Dependent structural changes in the secondary structures and in the hydrogen bondings of side chains, J. Phys. Chem. B 105 (2001) 4763–4769, https://doi.org/10.1021/jp004537a.
[66] K. Takeda, A. Wada, K. Yamamoto, Y. Moriyama, K. Aoki, Conformational change of bovine serum albumin by heat treatment, J. Protein Chem. 8 (1989) 653–659, https://doi.org/10.1007/BF01025605.
[67] P. Roach, D. Farrar, C.C. Perry, Surface tailoring for controlled protein adsorption: effect of topography at the nanometer scale and chemistry, J. Am. Chem. Soc. 128 (2006) 3939–3945, https://doi.org/10.1021/ja056278e.